Composites Part B 169 (2019) 148–156

Contents lists available at ScienceDirect

Composites Part B

journal homepage: www.elsevier.com/locate/compositesb

(3-aminopropyl) triethoxysilane grafted poly(dopamine)@Fe3O4 nanoparticles and their epoxy composites for functional application

Yang Zhang [a,b], Zhenqian Zhang [c], Jingyu Li [a,b], Guoxin Sui [a,b,*]

[a] Institute of Metal Research, Chinese Academy of Sciences, Shenyang, 110016, China
[b] School of Materials Science and Engineering, University of Science and Technology of China, Hefei, 230000, China
[c] Key Laboratory of Electromagnetic Processing of Materials (Ministry of Education), Northeastern University, Shenyang, 110819, China

ARTICLE INFO

Keywords:
Surface modification
Cube Fe_3O_4
Mechanical property
Thermal stability
Magnetic performance

ABSTRACT

The uniform dispersion of Fe_3O_4 nanoparticles and strong interfacial bonding with epoxy matrix are crucial for Fe_3O_4/epoxy composite with enhanced mechanical and thermal properties. Cube pure Fe_3O_4 nanoparticles (PF NPs) by poly (dopamine) (PDA) coated and (3-aminopropyl) triethoxysilane (APTES) grafted (PAF NPs) are successfully prepared via co-precipitation and seed polymerization method with an aim to enhance the dispersion and interfacial bonding with the epoxy matrix. The tensile strength of PAF/epoxy (1 wt%) increases from 57.8 MPa to 65.5 MPa (a rise scope of almost 13.3%) compared to pure epoxy. The thermal stabilities of PAF/epoxy composites with various PAF contents (1 wt%, 2 wt%, 3 wt%) are higher than that of pure epoxy. The saturation magnetization (Ms) of PAF/epoxy increases from 0.125 to 0.7 emu/g with PAF loading contents increasing from 0.5 to 3 wt%. The results suggest that dispersion and interfacial bonding of nanoparticles make a pivotal contribution to the enhanced performances of composites.

1. Introduction

As the versatile thermosetting polymer, epoxy resins have been extensively applied in different fields on account of thermal stability, chemical resistance, electrical insulating and excellent mechanical properties. In general, epoxy resins will lead to vulnerable defects like micropores and microcracks during curing process [1]. Great endeavors have been made to improve beneficial properties of epoxy resins by incorporating inorganic fillers including metal oxides [2,3], nanosilica [4] nanoclay [5,6], carbon nitride [7], boron nitride [8] and nanocarbon materials [9–11].

Magnetic polymer composites are stimuli-responsive smart materials which can accommodate their shape, displacement and structure in view of external magnetic field [12]. The magnetic properties and enhanced mechanical properties can be provided by incorporating pure Fe_3O_4 nanoparticles (PF NPs) into polymer matrix, which could broaden their engineered applications such as biomedical biosensors [13], excellent adhesives, protective coatings [14,15], structural materials [16,17], microwave adsorption [18], electromagnetic interference shielding [19–21], magnetic shape memory [22,23] and oil-water separation [24,25] due to the synergistic effect on both the non-conducting polymer matrix and magnetic nanoparticles. However, PF NPs are prone to aggregate because of the high surface area and strong dipole-dipole interaction [26]. Even, the intrinsic hydrophilic hydrogen bond of PF NPs leads to weak interphase interactions with organic polymers. Furthermore, they are susceptible to oxidize when exposed to the atmosphere [27]. Therefore, it is still an enormous challenge to carry out effective measures to functionalize PF NPs for enhancing the dispersion and interfacial adhesiveness with the polymer matrix.

Inspired by mussel-adhesive proteins, a controllable poly (dopamine) (PDA) coating can be spontaneously formed on various substrates under alkaline conditions [28–30]. On the one hand, functional groups including $-NH_2$ and $-OH$ from the PDA are adopted to enhance the attachment on the substrates. On the other hand, many active groups from PDA coating could supply a versatile platform with further surface modification [31–34]. (3-aminopropyl) triethoxysilane (APTES) is also utilized to improve the interphase adhesion with the matrix and dispersion of fillers, providing an alternative method to modify the substrates [35,36].

In this work, cube PF NPs by poly (dopamine) (PDA) coated and secondary monomer (APTES) grafted (PAF) were successfully prepared via co-precipitation and seed polymerization method. The PAF NPs were characterized by FTIR, XRD, DLS, Zeta potential and TEM. And the magnetic epoxy composites based on PAF NPs were fabricated. The

---

* Corresponding author. Institute of Metal Research, Chinese Academy of Sciences, Shenyang, 110016, China.
E-mail address: gxsui@imr.ac.cn (G. Sui).

https://doi.org/10.1016/j.compositesb.2019.04.012
Received 2 December 2018; Received in revised form 20 March 2019; Accepted 11 April 2019

thermal stability, mechanical property and magnetic performance of the as-prepared PAF/epoxy were studied in detail by SEM, TGA, DSC, tensile analysis, and vibrating sample magnetometer (VSM).

2. Experimental section

2.1. Material

Dopamine hydrochloride (DA) (98%) and tris (hydroxymethyl) aminomethane (99%) were purchased from Aladdin, China. Ferric chloride hexahydrate ($FeCl_3 \cdot 6H_2O$), Ferrous Sulfate heptahydrate ($FeSO_4 \cdot 7H_2O$), sodium hydroxide (NaOH), and (3-Aminopropyl) triethoxysilane (APTES) were purchased from Sinopharm Chemical Reagent Co. Ltd., China. The epoxy (E51) was purchased from Yueyang Petrochemical factory, China and its curing agent (Polyetheramine D230) was purchased from Shanghai Yuanmu Biotechnology Co. Ltd., China. All other reagents were purchased from commercial sources and utilized without further purification.

2.2. Fabrication of PF NPs

The PF NPs were fabricated by co-precipitation method as follows. Briefly, $FeCl_3 \cdot 6H_2O$ (2.7 g) and $FeSO_4 \cdot 7H_2O$ (1.4 g) (molar ratio = 2:1) were dissolved in deionized water (300 ml) for 10 min by ultrasonication at room temperature. After the solution was heated to 55 °C, total 40 ml of NaOH (1 mol/L) was then introduced dropwise to reach pH (10–11) under protective gas (N_2) with mechanical stirring. The mixture turned from light brown to brown and shiny bright color. Then suspension was heated to and maintained 60 °C for 1.5 h. After cooling down to room temperature, magnetic separation and wash with water several times should be done to get clean products.

2.3. Fabrication of PAF NPs with seed polymerization

In brief, PDA@Fe_3O_4 NPs were fabricated and applied as the seeds. PF (100 mg) and DA (10 mg) were dispersed in the tris butter solution (40 mg) to keep the pH = 8.5 by ultrasonication. After suspension was maintained at room temperature for 1 h under mechanical stirring, the mixture of DA (40 mg), APTES (10 mg), and tris butter (100 mg) solution were dropwise added to the flask for 30min, followed by co-polymerization reaction for 7 h at room temperature. Finally, the samples were obtained after magnetic separation rinsing with water several times.

2.4. Preparation of composites

The D230 suspension was fabricated by nanoparticles (PF NPs or PAF NPs) adding into the D230 by ultrasonication for 15 min. The epoxy composites were prepared by E51 and D230 suspension with various loading contents of nanoparticles (0 wt%, 1 wt%, 2 wt%, 3 wt%) under the mechanical stirring. The as-prepared epoxy composites were poured into the PTFE mold and heated at 80 °C (2 h), 120 °C (8 h) for the curing process.

2.5. Characterization

X-ray diffraction (XRD) patterns were achieved making use of the Rigaku Smartlab 9kw X-ray diffractometer. The PF NPs and PAF NPs were measured by Fourier transform infrared (FT-IR, NEXUS470, America). Diameters and zeta potential ofPF and PAF NPs were determined by the dynamic light scattering (DLS, ELS-Z, Japan) with zeta potential. The differential scanning calorimetry (DSC) was recorded by TA Q20. The thermogravimetric analysis (TGA) was tested by the TA Q500 under N_2 atmosphere. The SEM (FEI Inspect F50, America) and TEM (JEOL 2100F, Japan) were carried out to investigate the surfaces of PF NPs and PAF NPs. The cross-section morphologies of composites were observed by the SEM (JSM-6301F, Japan). Tensile properties of composites were measured by the WSM-20KN Electromechanical Universal Testing Machine. Magnetization measurements were measured at 3–350 K temperature range and under external magnetic fields up to 7 T taking advantage of a commercial vibrating sample magnetometer (VSM) by LAKESHORE.

3. Results and discussion

3.1. Modification of PF NPs

Fig. 1 shows a schematic of two-step approach to fabricate PAF NPs. Magnetic PF NPs are fabricated by co-precipitation, followed by modification via PDA and APTES. Thus, forming on the surface of PF NPs, the abundant amino groups and the thin layer of polymer-derivate can tightly connect with the epoxy matrix through chemical crosslinking reaction [37–39]. It has been confirmed that secondary functional monomer can further react with $-NH_2$ and $-OH$ groups of PDA for further grafting [40]. APTES is easily hydrolyzed into silanol with water, which can coexist with DA monomer in the solution. Thus, the bio-inspired co-modification [41] is achieved by self-polymerization process [42–44].

The characteristic peak at 573 cm^{-1} is assigned to the $Fe-O$ vibration (Fig. 2a), which also is caught sight of in PF NPs. Furthermore, the peak at 2922 cm^{-1} and 2851 cm^{-1} are corresponded to $-CH_2$ nonsymmetric and symmetric stretch vibration, respectively. The peak at 1514 cm^{-1} is attributed to the bending vibration of $-NH$ group [45]. More importantly, the peak at 1635 cm^{-1} is ascribed to the $C=N$ stretching vibration, indicating the successful reaction between DA and APTES through Schiff base reaction [46]. From these evidences of FT-IR spectra, it demonstrates PAF NPs are successfully fabricated.

The main characteristic peaks of two samples are exhibited at 2 θ = 18.30°, 30.12°, 35.40°, 37.10°, 43.10°, 53.51°, 57.01°, 62.62° and 74.10°, which correspond to the (111), (220), (311), (222), (400), (422), (511), (440) and (553) crystal planes, respectively (Fig. 2b) [26]. The XRD patterns show that the crystalline phase is not affected by surface modification. However, XRD pattern of PAF NPs compared with that of PF NPs become slightly weaker in terms of the intensity of peaks, as a result of PDA and $-NH_2$ attaching on PF NPs.

The XPS is performed to further investigate the surface structure of PF NPs and PAF NPs. Obviously, it can be observed that Fe2p, O1s and C1s exist in PF NPs from Fig. 3a and the peak of C1s may come from the impurities. The wide scan spectra of PAF shows the peak components of O1s, N1s, C1s, Si2s and Si2p, which are ascribed to the existence of O, N, C and Si elements in dopamine and APTES, respectively. Furthermore, the C1s peak of PAF NPs can be divided into six peaks where the bonding energies of 282.3 eV, 284.6 eV, 285.5 eV, 286.3 eV, 287.2 eV and 288.3 eV are responsible for $C-Si$, $C-C$, $C-N$, $C=N$, $C-OH$ and $C=O$ respectively (Fig. 3b) [26]. The existence of $C-Si$ species are confirmed the incorporation of APTES into the PAF. The $C=N$ species are corresponding to the chemical reaction between dopamine and APTES [1] which is consistent with the results from FT-IR (Fig. 2a). Therefore, the core-shell structured PAF NPs are successfully prepared confirmed by all the above esults.

3.2. Morphology of nanoparticles

Fig. 4 exhibits SEM, TEM images of PF NPs at various magnifications, TEM images of PAF NPs at various magnifications and SAED pattern of PAF NPs. The PF NPs are stacked tightly with high aggregation owing to high surface energy (Fig. 4a). Cube PF NPs with smooth surface are estimated to be 15–20 nm (Fig. 4b). However, after functionalization with PDA and APTES, the surface of PAF NPs become relatively rough ascribing to thin PDA layer and abundant $-NH_2$ from the APTES, preventing the stacking and aggregation of PAF NPs (Fig. 4d). Moreover, a densely thin layer is wrapped on the PF NP with an average thickness

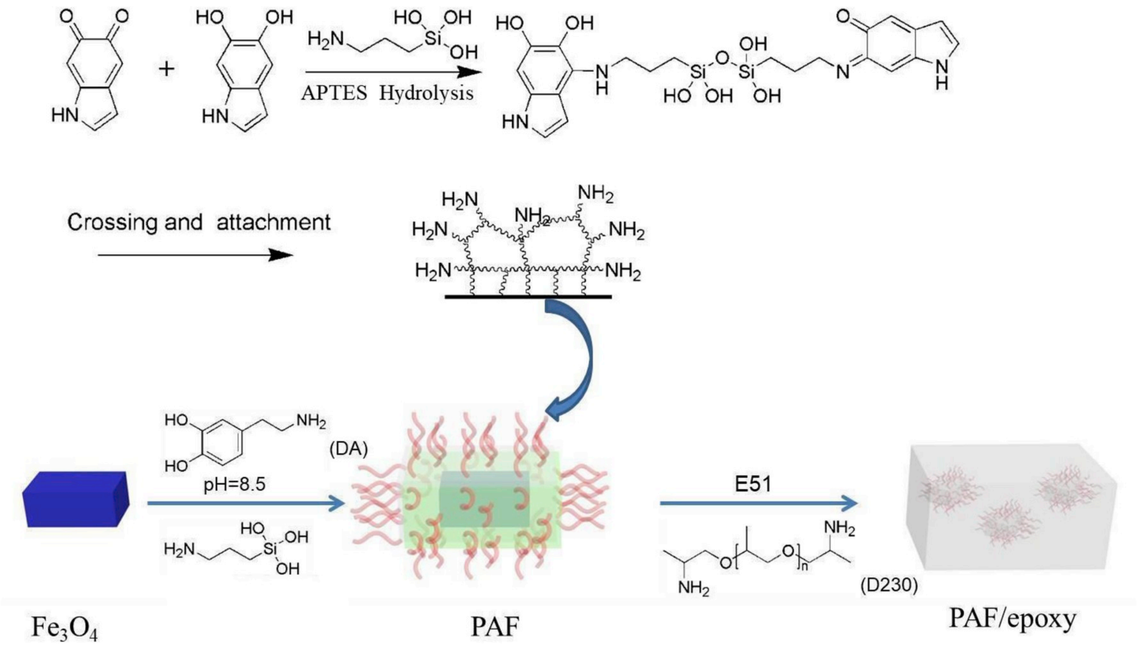

Fig. 1. Scheme of the PAF/epoxy composite.

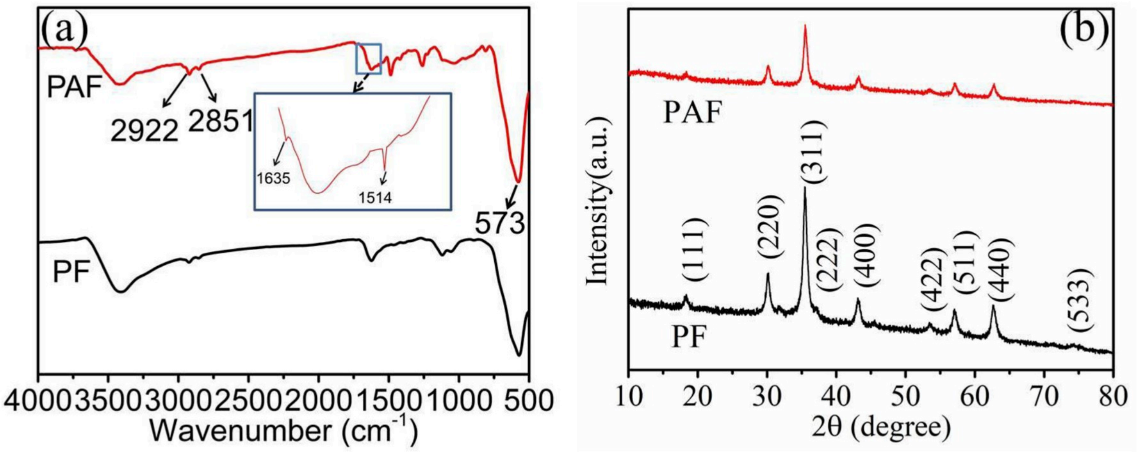

Fig. 2. (a) FT-IR spectra of PF NPs and PAF NPs and (b) XRD patterns of PF NPs and PAF NPs.

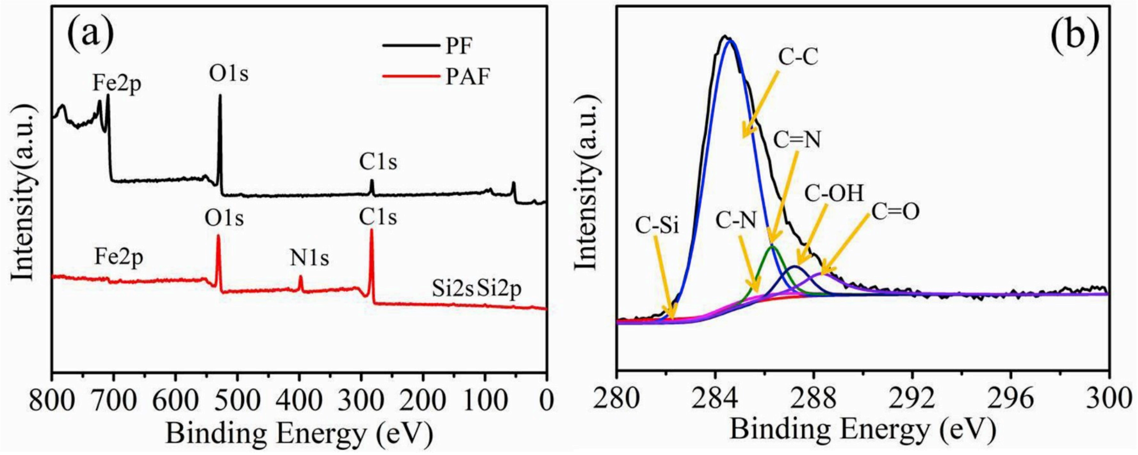

Fig. 3. XPS wide scan (a) and C1s spectra (b) of PAF NPs.

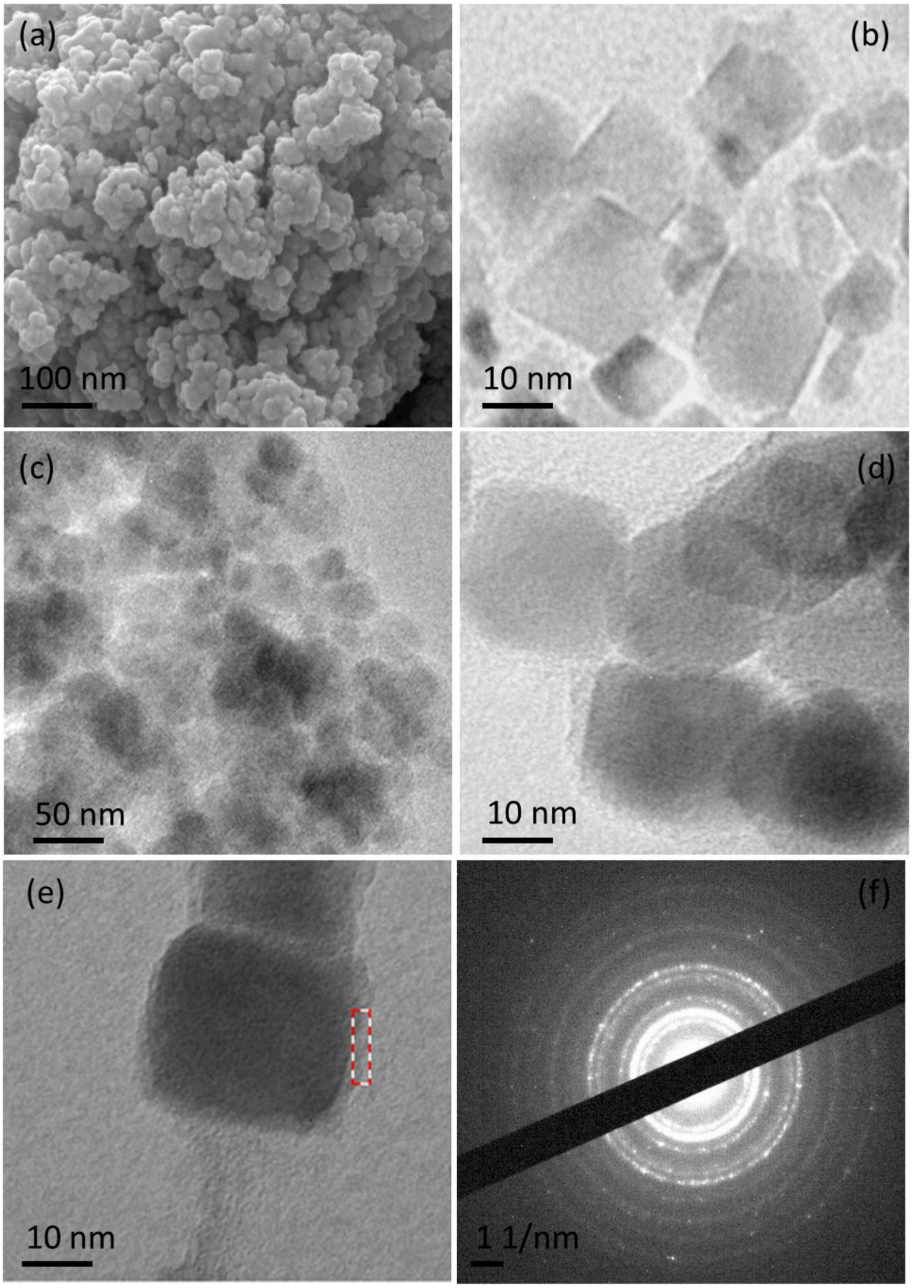

Fig. 4. (a) SEM image of PF NPs, (b) TEM image of several PF NPs, (c) and (d) TEM image of the PAF NPs at various magnifications, (e) TEM image of a single PAF NP, (f) SAED pattern of the PAF NPs.

about 3 nm (Fig. 4e). The continuous rings and corresponding intensities show the polycrystalline nature of PAF NPs resulting from the incorporation of the PF NPs (Fig. 4f).

3.3. *Mean hydrodynamic diameter and polydispersity index of nanoparticles*

Mean hydrodynamic diameter and polydispersity index (PDI) of the PF as well as PAF NPs are measured by dynamic light scattering (DLS). After dispersion in water for 5 min, the PF NPs have bigger mean diameter of 568 ± 234.53 nm (Fig. 5a) than 312 ± 31.7 nm of PAF NPs (Fig. 5b). The PF NPs are susceptible to be aggregations as the result of high surface energy and magnetic dipole-dipole interactions [47]. PAF NPs exhibit excellent dispersion owing to PDA thin layer forming on the surface of PF NPs and strong repulsion effect from —NH_2. The zeta potential of the PF NPs is 14.23 mv attributing to high isopotential point (>7) [48], while the zeta potential of PAF NPs is −18.4 mv owing to the amine groups and phenolic hydroxyl groups from PDA [49].

3.4. *Fracture surface of composites by SEM*

The SEM of fracture surface can clearly explain the dispersion of particles in the matrix. The tensile fracture surface of pure epoxy, PF/epoxy (1 wt%) and PAF/epoxy (1 wt%) are presented in Fig. 6. It can be seen the pure epoxy exhibits relatively smooth river-shaped fracture surface (Fig. 6a), indicating the brittle fracture of the epoxy resin. However, a considerable number of random river-shaped lines and much more rougher fracture cracks have been observed (Fig. 6b and c), which can be ascribed to the matrix tensile yielding interrupted by the nanoparticles [50]. It exhibits that PAF NPs are more homogeneously dispersed in the epoxy matrix compared to PF NPs (Fig. 6c). This better dispersion is due to relatively excellent dispersion of PAF NPs and strong

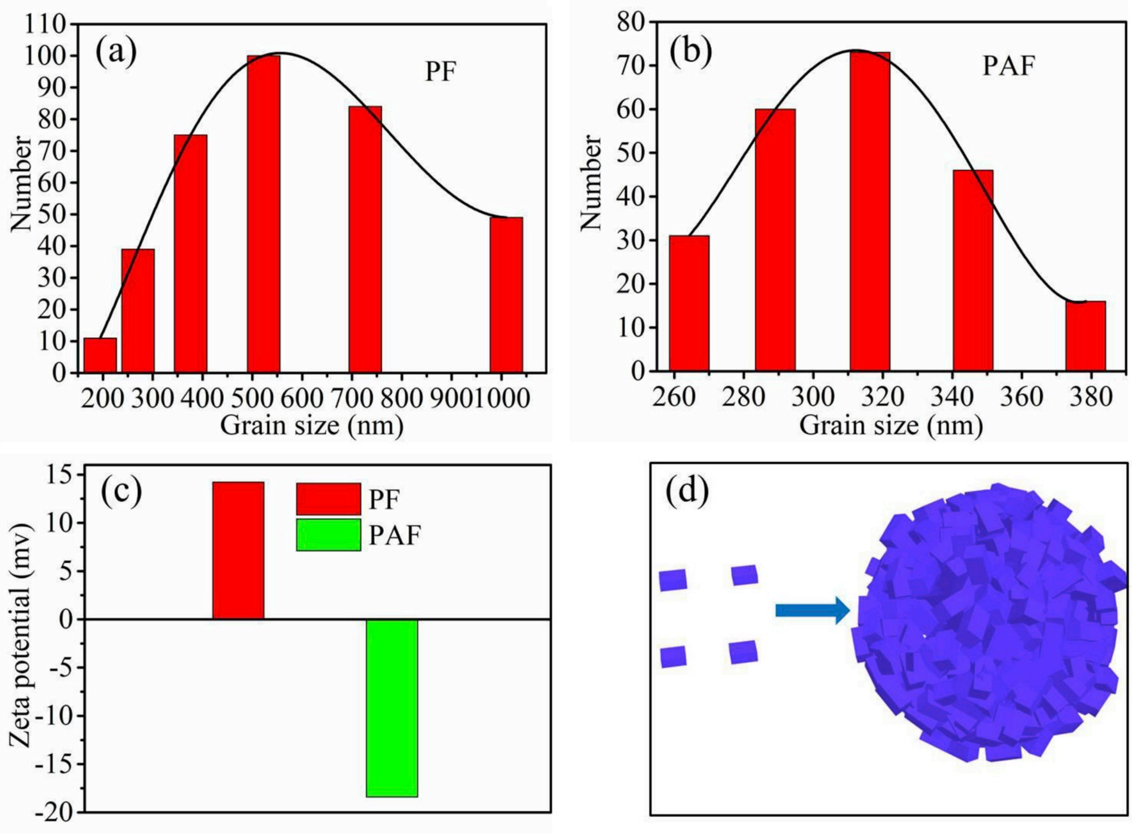

Fig. 5. Mean hydrodynamic diameter and PDI of (a) PF NPs and (b) the PAF NPs aggregation in water after 5 min. (c) The zeta potential of PF NPs and the PAF NPs at pH = 7. (d) Schematic illustration exhibiting the formation of cube PF NPs aggregation in water.

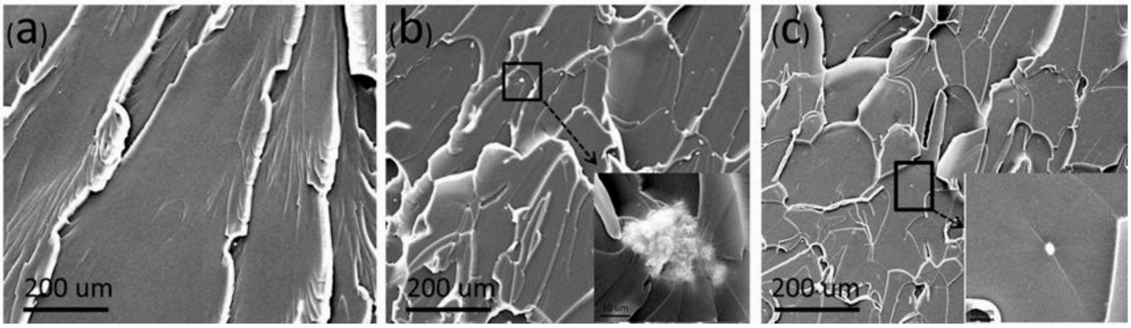

Fig. 6. SEM images of the tensile fracture surface (a) pure epoxy, (b) PF/epoxy (1 wt%) and (c) the PAF/epoxy (1 wt%).

interphase interactions between —NH_2 forming on PAF NPs with epoxy chains during fabrication of composites. Owing to hydrogen bonds formation between epoxy matrix and hydroxyl groups on the face of PF NPs [51], the PF/epoxy exhibits increase in more agglomerated particles sizes and quantity in comparison with PAF/epoxy (Fig. 6b).

3.5. Tensile test

The mechanical properties of composites are investigated by tensile test. Fig. 7 and Table 1 show the tensile strengths and Young's modulus of pure epoxy, PF/epoxy and PAF/epoxy composites. Electrostatic interaction and hydrogen bond are the major forms between D230 molecules and the adsorbent surface of nanoparticles. It can be clearly observed that the tensile property can be effectively enhanced by embedding PAF NPs into epoxy matrix (Fig. 7 and Table 1). In comparison with pure epoxy, the average tensile strength of PF/epoxy is improved from 57.8 MPa to 58.7 MPa, (a rise scope of almost 2%). Compared to the pure epoxy, the Young's modulus of PF/epoxy is enhanced from 2.4 GPa to 2.7 GPa with 13.3% enhancement, owing to incorporating the rigid PF NPs. The PF/epoxy displays poor tensile strength (58.7 MPa) compared to the modified sample (65.5 MPa), owing to weak interface interactions of highly agglomerated particles [52] (Fig. 6b), and thus localization of stresses applied at less interface area compared to the modified samples [51]. The superior tensile strength of PAF/epoxy increases from 57.8 MPa to 65.5 MPa compared to pure epoxy, which is assigned to the strong interfacial interactions between covalent bonding (NH_2 group) of PAF and epoxy matrix, leading to localization of mechanical stresses at the broad interface [53].

3.6. Thermal property of composites

The thermal stabilities of pure epoxy and PAF/epoxy composites

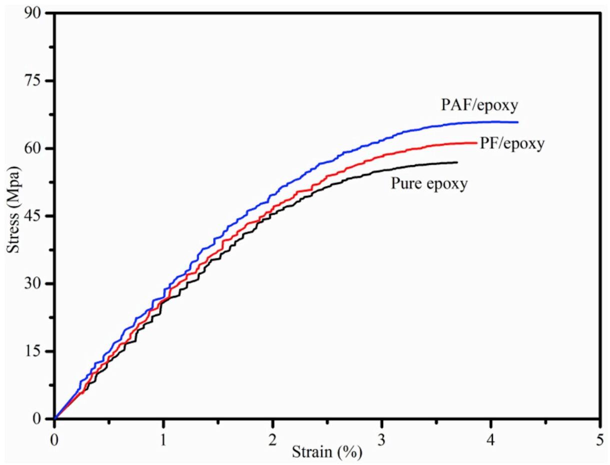

Fig. 7. Stress-Strain curves of pure epoxy, PF/epoxy (1 wt%) and PAF/epoxy (1 wt%) composites.

Table 1
Mechanical properties of pure epoxy, PF/epoxy (1 wt%) and PAF/epoxy composites (1 wt%).

Code	Filler content (wt %)	Tensile strength (MPa)	Young's modulus (GPa)
Pure epoxy	0	57.8 ± 1.95	2.4 ± 0.012
PF/epoxy	1	58.7 ± 2.1	2.7 ± 0.14
PAF/ epoxy	1	65.5 ± 0.96	2.7 ± 0.061

with PAF NPs loading contents (1 wt%, 2 wt%, 3 wt%) are measured by TGA under nitrogen atmosphere. The thermal decomposition temperature of 5% weight loss ($T_{5\%}$), 50% weight loss ($T_{50\%}$), maximum weight loss (T_{max}) and residue (Tr) are presented in Fig. 8a and summed up in Table 2. The thermal stabilities of composites are enhanced with the incorporation of PAF NPs. The $T_{5\%}$, $T_{50\%}$, T_{max} and Tr of pure epoxy are lower than that of any other samples with incorporation of PAF NPs. $T_{50\%}$ of PAF/epoxy (3 wt%) is higher 20 °C (373 °C) than that of pure epoxy (353 °C). Besides, the Tr of composites at 700 °C are gradually increased with the additional PAF loading contents, from 7.51% (pure epoxy) to 9.51% (PAF (3 wt%)), respectively. The thermal stabilities of composites are associated with the barrier effect of PAF NPs, retarding the gas evolution and weight loss [51].

Fig. 8b exhibits the glass transition temperature (T_g) of pure epoxy and PAF/epoxy composites. In the case of the pure epoxy, T_g is evaluated at about 78 °C. It is noteworthy that the T_g of PAF/epoxy (1 wt%) reach the maximum value (85 °C) which is a critical point of composites and then decrease gradually with the further incorporation of PAF loading contents. This phenomenon is attributed to two reasons. On the one hand, PAF NPs play a pivotal role in the epoxy matrix as the crosslinking point that can effectively make for entanglement in epoxy chain and block the movement of the epoxy chains. On the other hand, the polymer-derivate forming on the surface of PF NPs grafting PDA and APTES results in strong interphase interactions between PAF NPs and epoxy matrix, leading to higher T_g compared with the pure epoxy. However, the T_g of PAF/epoxy (2 wt%) is evaluated at about 75 °C while T_g of PAF/epoxy (3 wt%) decreases to 72 °C. This can be assigned to that partially agglomerated particles reduce the crosslinking degree of curing system, leading to a corresponding decrease in the T_g.

Table 2
Thermal properties of PF/epoxy and PAF/epoxy composites.

Samples	0 wt%	1 wt%	2 wt%	3 wt%
T_g (°C)	78	85	75	73
$T_{5\%}$ (°C)	300	330	333	335
$T_{50\%}$ (°C)	353	365	370	373
T_{max} (°C)	350	363	358	365
T_r (%)	7.51	8.63	9.08	9.51

3.7. Magnetic property

The investigation about the temperature dependent on magnetization has been measured by the zero field-cool (ZFC) and field-cool (FC) protocol. It can be seen from Fig. 9a–d that ZFC and FC curves, which present different trend initially, carry out gradually to be close as the temperature increases from 0 to 343 K. Generally, the ZFC curve exhibits a maximum temperature named as T_{MAX} which is associated with superparamagnetic behavior [54]. The blocking temperature values (T_B) evaluated from the ZFC maximum ($T_{MAX} = T_B$) are found to be 211, 343, 192, and 40.6 K at different H from 5 to 5000 Oe, respectively (Fig. 9a–d).

The spins glass-like behavior is resultant from surface spins of the particles. The ZFC-FC magnetization is measured to investigate the spin freezing effect at different applied field H. The curve of d (m_{zfc}-m_{fc})/dt versus T is plotted to explain the spin freezing effect (Fig. 9e and f) [55]. Two different curves are signed as Peak 1 and Peak 2, respectively. The existence of the Peak 2 can be assigned to the blocking temperature of PAF NPs. The Peak 2 has the T_B about 343 K for H = 50 Oe and disappears for H = 5000 Oe. Meanwhile, the appearance of Peak 1 can be ascribed to freezing effect of the surface spins of these nanoparticles. It is clearly observed that the freezing of the spin glass-like surface spins

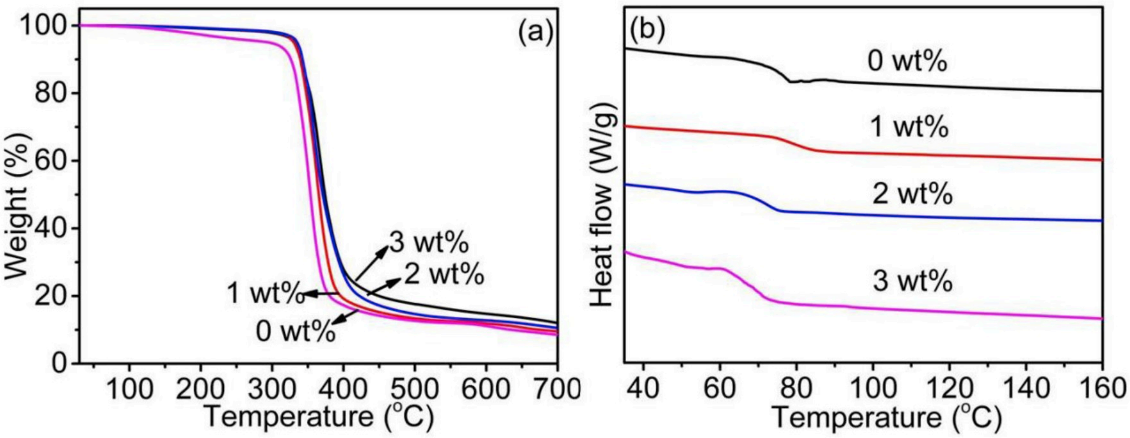

Fig. 8. TGA (a) and DSC (b) curves of pure epoxy and PAF/epoxy composites.

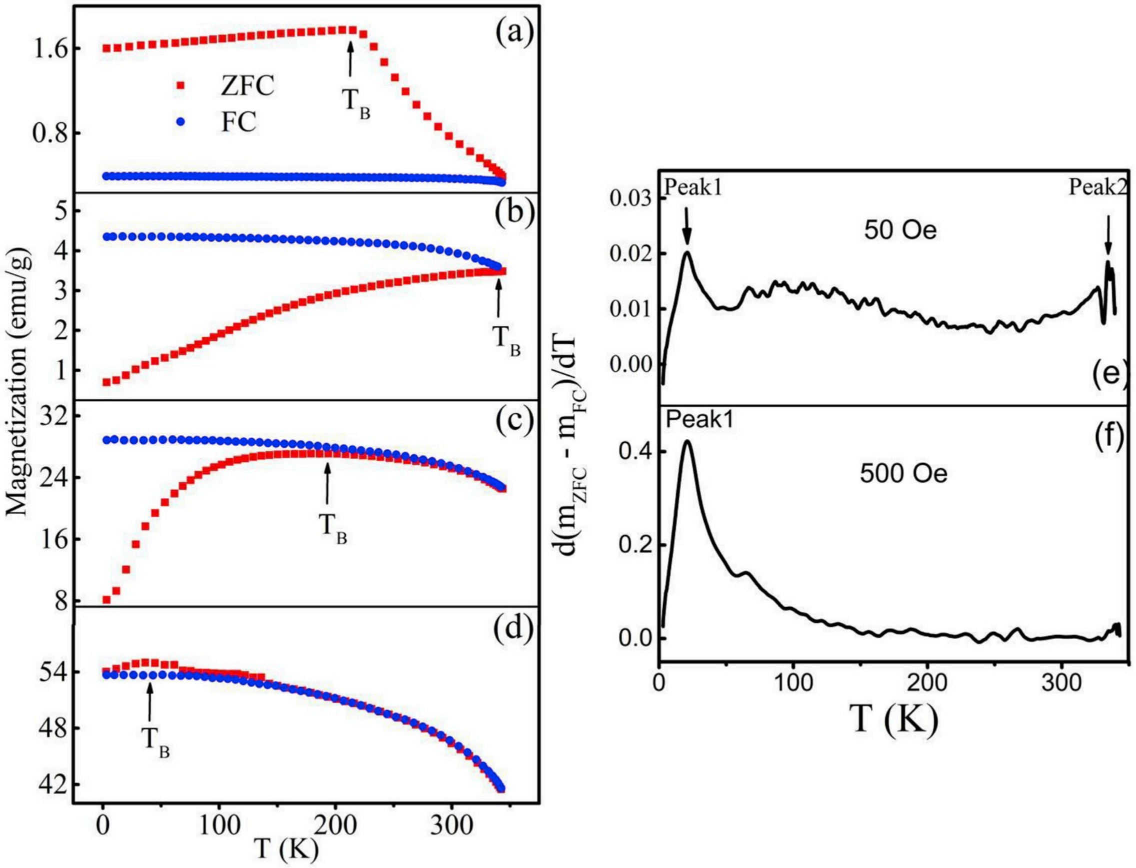

Fig. 9. ZFC-FC magnetization curves of the PAF powder at different H (a) 5 Oe, (b) 50 Oe, (c) 500 Oe, (d) 5000 Oe, (e–f) d (m_{ZFC}-m_{FC})/dT versus T from (b)–(c).

occurs on the temperature below 50 K in Peak 1. The Peak 1 gets obvious with the increasing H which is owing to the frozen fraction of surface spins along the direction of the increasing applied field.

Fig. 10a displays M − H loop of PAF NPs at 300 K under field of ±7 T. The inset exhibits enlarged region of the coercivity (*Hc*) which represents the ability of a material to retain external magnetic field without demagnetize [56]. The value of H_C and saturation magnetization (M_S) are 48 Oe and 44.8 emu/g, respectively (Fig. 10a). The magnetic properties of PAF/epoxy with different loading contents are investigated in the range of applied fields between -7T and 7T at 300 K. The M_S of PAF/epoxy increases from 0.125 to 0.7 emu/g with increasing PAF loading contents from 0.5 to 3 wt% (Fig. 10b). Magnetization defines in response to the induced magnetic dipole moments in a magnetics material to an external magnetic field [50]. When the magnet is placed beside the bottle having a piece of PAF/epoxy composite, the composite quickly moves along the magnetic field. The experimental phenomenon reflects that the magnetism of PAF/epoxy composite is derived from PAF NPs.

4. Conclusions

The PAF NPs by poly (dopamine) (PDA) coated and secondary

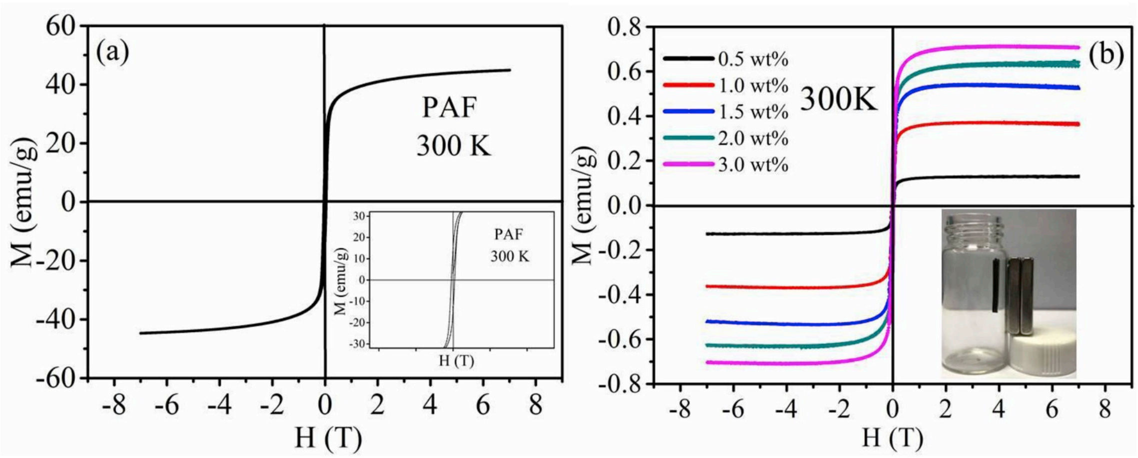

Fig. 10. (a) M − H loop of PAF NPs at 300 K. The inset shows an expanded view of the magnetic hysteresis loop (b) M − H loops of the PAF/epoxy composites with various PAF loading contents at 300 K. Magnetic response is exhibited under an external magnetic field at bottom right inset.

monomer (APTES) grafted have been prepared with the co-precipitation and seed polymerization method, which are confirmed by FT-IR, XRD, DLS, Zeta potential and TEM. Compared to pure epoxy, the mechanical property and thermal stability of PAF/epoxy have been enhanced owing to strong interphase interaction and well dispersion with the epoxy matrix. Typically, the tensile strength of PAF/epoxy (1 wt%) increases from 57.8 MPa to 65.5 MPa (a rise scope of almost 13.3%) compared to pure epoxy. The thermal stabilities of PAF/epoxy composites with various PAF contents (1 wt%, 2 wt%, 3 wt%) are higher than that of pure epoxy. The saturation magnetization (Ms) of PAF/epoxy increases from 0.125 to 0.7 emu/g with PAF loading contents increasing from 0.5 to 3 wt%. Taking their exceptional performances into consideration, the composites will have broad applications in the engineering fields.

References

[1] Zhan Y, Zhang J, Wan X, Long Z, He S, He Y. Epoxy composites coating with Fe_3O_4 decorated graphene oxide: modified bio-inspired surface chemistry, synergistic effect and improved anti-corrosion performance. Appl Surf Sci 2018;436:756–67.

[2] Yao DD, Peng NK, Zheng YP. Enhanced mechanical and thermal performances of epoxy resin by oriented solvent-free graphene/carbon nanotube/Fe_3O_4 composite nanofluid. Compos Sci Technol 2018;167:234–42.

[3] Prolongo SG, Meliton BG, Del Rosario G, Urena A. New alignment procedure of magnetite-CNT hybrid nanofillers on epoxy bulk resin with permanent magnets. Compos B Eng 2013;46:166–72.

[4] Alsaadi M, Bulut M, Erklig A, Jabbar A. Nano-silica inclusion effects on mechanical and dynamic behavior of fiber reinforced carbon/Kevlar with epoxy resin hybrid composites. Compos B Eng 2018;152:169–79.

[5] Sun Y, Liu Y, Jiang Y, Xu K, Xi Z, Xie H. Thermal and mechanical properties of natural fibrous nanoclay reinforced epoxy asphalt adhesives. Int J Adhesion Adhes 2018;85:308–14.

[6] Bozkurt OY, Bulut M, Erklig A, Faydh WA. Axial and lateral buckling analysis of fiber reinforced S-glass/epoxy composites containing nano-clay particles. Compos B Eng 2019;158:82–91.

[7] Song B, Wang T, Wang L, Liu H, Mai X, Wang X, et al. Interfacially reinforced carbon fiber/epoxy composite laminates via in-situ synthesized graphitic carbon nitride ($g\text{-}C_3N_4$). Compos B Eng 2019;158:259–68.

[8] Lee Jae-Ha, Shin Hyunho, Rhee Kyong Yop. Surface functionalization of boron nitride platelets via a catalytic oxidation/silanization process and thermomechanical properties of boron nitrideepoxy composites. Compos B Eng 2019;157:276–82.

[9] Shen JT, Buschhorn ST, De Hosson JTM, Schulte K, Fiedler B. Pressure and temperature induced electrical resistance change in nano-carbon/epoxy composites. Compos Sci Technol 2015;115:1–8.

[10] Wang Q, Wen GD, Chen JN, Su DS. Reinforcing epoxy resin with nitrogen doped carbon nanotube: a potential lightweight structure material. J Mater Sci Technol 2018;34(11):2205–11.

[11] Vedrtnam A. Novel method for improving fatigue behavior of carbon fiber reinforced epoxy composite. Compos B Eng 2019;157:305–21.

[12] Moscoso-Londoño O, Tancredi P, Muraca D, Zélis PM, Coral D, Raap MBFV, et al. Different approaches to analyze the dipolar interaction effects on diluted and concentrated granular superparamagnetic systems. J Magn Magn Mater 2017;428:105–18.

[13] Zhu W, Khan MS, Wei C, Xu S, Ma H, Yong Z, et al. $Ni(OH)_2$/NGQDs-based electrochemiluminescence immunosensor for prostate specific antigen detection by coupling resonance energy transfer with $Fe_3O_4@MnO_2$ composites. Biosens Bioelectron 2018;99:346–52.

[14] Zhang C, He Y, Xu Z, Shi H, Di H, Pan Y, et al. Fabrication of $Fe_3O_4@SiO_2$ nanocomposites to enhance anticorrosion performance of epoxy coatings. Polym Adv Technol 2016;27(6):740–7.

[15] Zhang C, He Y, Li F, Di H, Zhang L, Zhan Y. h-BN decorated with Fe_3O_4 nanoparticles through mussel-inspired chemistry of dopamine for reinforcing anticorrosion performance of epoxy coatings. J Alloy Comp 2016;685:743–51.

[16] He Y, Chen Q, Yang S, Lu C, Feng M, Jiang Y, et al. Micro-crack behavior of carbon fiber reinforced Fe_3O_4/graphene oxide modified epoxy composites for cryogenic application. Compos Appl Sci Manuf 2018;108:12–22.

[17] Irez AB, Bayraktar E, Miskioglu I. Recycled and devulcanized rubber modified epoxy-based composites reinforced with nano-magnetic iron oxide, Fe_3O_4. Compos B Eng 2018;148:1–13.

[18] Qiao M, Lei X, Ma Y, Tian L, Su K, Zhang Q. Dependency of tunable microwave absorption performance on morphology-controlled hierarchical shells for core-shell $Fe_3O_4@MnO_2$ composite microspheres. Chem Eng J 2016;304:552–62.

[19] Chen Y, Wang Y, Zhang HB, Li X, Gui CX, Yu ZZ. Enhanced electromagnetic interference shielding efficiency of polystyrene/graphene composites with magnetic Fe_3O_4 nanoparticles. Carbon 2015;82:67–76.

[20] He Y, Lu L, Sun K, Wang F, Hu S. Electromagnetic wave absorbing cement-based composite using Nano-Fe_3O_4 magnetic fluid as absorber. Cement Concr Compos 2018;92:1–6.

[21] Liu Y, Song D, Wu C, Leng J. EMI shielding performance of nanocomposites with MWCNTs, nanosized Fe_3O_4 and Fe. Compos B Eng 2014;63:34–40.

[22] Xia S, Li X, Wang Y, Pan Y, Zheng Z, Ding X, et al. A remote-activated shape memory polymer network employing vinyl-capped Fe_3O_4 nanoparticles as netpoints for durable performance. Smart Mater Struct 2014;23(8), 085005.

[23] Feng XQ, Zhang GZ, Bai QM, Jiang HY, Xu B, Li HJ. High strength self-healing magnetic elastomers with shape memory effect. Macromol Mater Eng 2016;301(2):125–32.

[24] Su X, Li H, Lai X, Zhang L, Liao X, Wang J, et al. Dual-functional superhydrophobic textiles with asymmetric roll-down/pinned states for water droplet transportation and oil-water separation. ACS Appl Mater Interfaces 2018;10(4):4213–21.

[25] Li ZT, Lin B, Jiang LW, Lin EC, Chen J, Zhang SJ, et al. Effective preparation of magnetic superhydrophobic Fe_3O_4/PU sponge for oil-water separation. Appl Surf Sci 2018;427:56–64.

[26] Wan X, Zhan Y, Long Z, Zeng G, Ren Y, He Y. High-performance magnetic poly (arylene ether nitrile) nanocomposites: co-modification of Fe_3O_4 via mussel inspired poly(dopamine) and amino functionalized silane KH550. Appl Surf Sci 2017;425:905–14.

[27] Chen L, Xu Z, Dai H, Zhang S. Facile synthesis and magnetic properties of monodisperse Fe3O4/silica nanocomposite microspheres with embedded structures via a direct solution-based route. J Alloy Comp 2010;497(1):221–7.

[28] Wang N, Wang Y, Shang B, Wen P, Peng B, Deng Z. Bioinspired one-step construction of hierarchical superhydrophobic surfaces for oil/water separation. J Colloid Interface Sci 2018;531:300–10.

[29] Jing X, Mi HY, Napiwocki BN, Peng XF, Turng LS. Mussel-inspired electroactive chitosan/graphene oxide composite hydrogel with rapid self-healing and recovery behavior for tissue engineering. Carbon 2017;125:557–70.

[30] Wan X, Zhan Y, Long Z, Zeng G, He Y. Core@double-shell structured magnetic halloysite nanotube nano-hybrid as efficient recyclable adsorbent for methylene blue removal. Chem Eng J 2017;330:491–504.

[31] Wu K, Song X, Cui S, Li Z, Jiao Y, Zhou C. Immobilization of bovine serum albumin via mussel-inspired polydopamine coating on electrospun polyethersulfone (PES) fiber mat for effective bilirubin adsorption. Appl Surf Sci 2018;451:45–55.

[32] Wang W, Li R, Tian M, Liu L, Zou H, Zhao X, et al. Surface silverized meta-aramid fibers prepared by bio-inspired poly(dopamine) functionalization. ACS Appl Mater Interfaces 2013;5(6):2062–9.

[33] Zhang X, Huang Q, Deng F, Huang H, Wan Q, Liu M, et al. Mussel-inspired fabrication of functional materials and their environmental applications: progress and prospects. Appl Mater Today 2017;7:222–38.

[34] Liu Y, Ai K, Lu L. Polydopamine and its derivative materials: synthesis and promising applications in energy, environmental, and biomedical fields. Chem Rev 2014;114(9):5057–115.

[35] Li Z, Liu B, Kong H, Yu M, Qin M, Teng C. Layer-by-Layer self-assembly strategy for surface modification of aramid fibers to enhance interfacial adhesion to epoxy resin. Polymer 2018;10(8):820.

[36] Fan B, Liu Y, He D, Bai J. Enhanced thermal conductivity for mesophase pitch-based carbon fiber/modified boron nitride/epoxy composites. Polymer 2017;122:71–6.

[37] Huang Q, Liu M, Mao L, Xu D, Zeng G, Huang H, et al. Surface functionalized SiO_2 nanoparticles with cationic polymers via the combination of mussel inspired chemistry and surface initiated atom transfer radical polymerization: characterization and enhanced removal of organic dye. J Colloid Interface Sci 2017;499:170–9.

[38] Huang Q, Liu M, Chen J, Wan Q, Tian J, Huang L, et al. Facile preparation of MoS_2 based polymer composites via mussel inspired chemistry and their high efficiency for removal of organic dyes. Appl Surf Sci 2017;419:35–44.

[39] Zhang XY, Huang Q, Liu MY, Tian JW, Zeng GJ, Li Z, et al. Preparation of amine functionalized carbon nanotubes via a bioinspired strategy and their application in Cu^{2+} removal. Appl Surf Sci 2015;343:19–27.

[40] Rina S, Yan Y, Zhenhai W, Liqun Z, Wencai W, Ming T. Surface modification of aramid fibers by bio-inspired poly(dopamine) and epoxy functionalized silane grafting. ACS Appl Mater Interfaces 2014;6(23):21730–8.

[41] Huang L, Liu M, Huang H, Wen Y, Zhang X, Wei Y. Recent advances and progress on melanin-like materials and their biomedical applications. Biomacromolecules 2018;19(6):1858–68.

[42] Liu M, Zeng G, Wang K, Wan Q, Tao L, Zhang X, et al. Recent developments in polydopamine: an emerging soft matter for surface modification and biomedical applications. Nanoscale 2016;8(38):16819–40.

[43] Zhang XY, Wang SQ, Xu LX, Feng L, Ji Y, Tao L, et al. Biocompatible polydopamine fluorescent organic nanoparticles: facile preparation and cell imaging. Nanoscale 2012;4(18):5581–4.

[44] Zeng G, Huang L, Huang Q, Liu M, Xu D, Huang H, et al. Rapid synthesis of MoS_2-PDA-Ag nanocomposites as heterogeneous catalysts and antimicrobial agents via microwave irradiation. Appl Surf Sci 2018;459:588–95.

[45] Cui JY, Zhou ZP, Xie AT, Meng MJ, Cui YH, Liu SW, et al. Bio-inspired fabrication of superhydrophilic nanocomposite membrane based on surface modification of SiO_2 anchored by polydopamine towards effective oil-water emulsions separation. Separ Purif Technol 2019;209:434–42.

[46] Shi H, He Y, Pan Y, Di HH, Zeng GY, Zhang L, et al. A modified mussel-inspired method to fabricate TiO_2 decorated superhydrophilic PVDF membrane for oil/water separation. J Membr Sci 2016;506:60–70.

[47] Chin SF, Makha M, Raston CL, Saunders M. Magnetite ferrofluids stabilized by sulfonato-calixarenes. Chem Commun 2007;19:1948–50.

[48] Qiu Y, Guo H, Guo C, Zheng J, Yue T, Yuan Y. One-step preparation of nano-Fe_3O_4 modified inactivated yeast for the adsorption of patulin. Food Control 2018;86:310–8.

[49] Yu B, Liu J, Liu S, Zhou F. Pdop layer exhibiting zwitterionicity: a simple electrochemical interface for governing ion permeability. Chem Commun 2010;46 (32):5900–2.
[50] Gu H, Tadakamalla S, Huang Y, Colorado HA, Luo Z, Haldolaarachchige N, et al. Polyaniline stabilized magnetite nanoparticle reinforced epoxy nanocomposites. ACS Appl Mater Interfaces 2012;4(10):5613–24.
[51] Mohammadi A, Barikani M, Doctorsafaei AH, Isfahani AP, Shams E, Ghalei B. Aqueous dispersion of polyurethane nanocomposites based on calix[4]arenes modified graphene oxide nanosheets: preparation, characterization, and anti-corrosion properties. Chem Eng J 2018;349:466–80.
[52] Zec J, Tomic NZ, Zrilic M, Levic S, Marinkovic A, Heinemann RJ. Optimization of Al_2O_3 particle modification and UHMWPE fiber oxidation of EVA based hybrid composites: compatibility, morphological and mechanical properties. Compos B Eng 2018;153:36–48.
[53] Mohammadi A, Barikani M, Lakouraj MM. Biocompatible polyurethane/thiacalix [4]arenes functionalized Fe_3O_4 magnetic nanocomposites: synthesis and properties. Mater Sci Eng C 2016;66:106–18.
[54] Kondrat'Eva ON, Nikiforova GE, Tyurin AV, Shevchenko EV, Andrusenko EV, Smirnova MN, et al. Thermodynamic and magnetic properties of magnesium-gallium ferrite ceramics. Ceram Int 2018;44(4):4367–74.
[55] Shameem PVM, Kumar MS. Training effect of the exchange bias in sputter deposited Fe_3O_4 thin films with varying thickness. J Magn Magn Mater 2018;458: 241–52.
[56] Zhan YH, Wang J, Zhang KY, Li YC, Meng YY, Yan N, et al. Fabrication of a flexible electromagnetic interference shielding Fe_3O_4@reduced graphene oxide/natural rubber composite with segregated network. Chem Eng J 2018;344:184–93.